SUPPLEMENTARY INFORMATION:

Unusually low and density-insensitive thermal conductivity of three-dimensional gyroid graphene

Gang Seob Jung[1], Jingjie Yeo[1,3], Zhiting Tian[4], Zhao Qin[1], Markus J. Buehler[1, 2]

[1] Laboratory for Atomistic and Molecular Mechanics (LAMM), Department of Civil and Environmental Engineering, Massachusetts Institute of Technology, 77 Massachusetts Ave., Cambridge 02139, MA, USA

[2] Center for Computational Engineering, Massachusetts Institute of Technology, 77 Massachusetts Ave., Cambridge, MA 02139, USA

[3] Institute of High Performance Computing, A*STAR, 1 Fusionopolis Way, #16-16 Connexis, Singapore, 138632, Singapore

[4]Department of Mechanical Engineering, Virginia Tech, 635 Prices Fork Rd, Blacksburg, VA 24061

Models of periodic gyroid graphene

All atomistic simulations and modeling are performed on the Large-scale Atomic/Molecular Massively Parallel Simulator (LAMMPS) package[1]. We utilize the graphene gyroid models proposed in a previous study[2], where the gyroid shape of graphene is made based on several steps. Here, we briefly introduce the method: Firstly, we obtain triangular flakes from Lennard-Jones particles with an external potential that allows the particles to form gyroid geometries. Secondly, particles are deleted to form hexagonal flakes based on the bond numbers. Finally, the geometries are refined with interatomic interactions based on the Adaptive Intermolecular Reactive Empirical Bond Order (AIREBO) Potential[3, 4] together with the external potential. Boundary atoms of flakes are added or deleted based on the bond number with a modified switching function cutoff of 2.0Å. This cutoff is important for natural behaviors of bond breaking and forming with the REBO potential[5, 6]. The generated models are shown in Figure 1. The x-, y-, and z-coordinates of the atoms are generated according to the equation

$$\sin\left(2\pi\frac{x}{L}\right)\cos\left(2\pi\frac{y}{L}\right)+\sin\left(2\pi\frac{y}{L}\right)\cos\left(2\pi\frac{z}{L}\right)+\sin\left(2\pi\frac{z}{L}\right)\cos\left(2\pi\frac{x}{L}\right)=0, \quad \text{(S1)}$$

where L is a parameter for the lattice constant of a unit cell. In this study, we test the thermal conductivities of five different atomistic models with different sizes (L: from 3 to 20nm). It is important to note that the curvature of the shape is induced by pentagon and heptagon defects (the disorder ratio, β, is shown in Table S1). Unlike 2D polycrystalline graphene, the pentagon-heptagon rings induce dislocations and thus, various curvatures.

For the thermal properties, the selection of interatomic potentials is critical for the reliable behaviors of systems. Although AIREBO is proper to build the models by processes including bond forming and breakings, Tersoff potential has been widely used in thermal MD studies for carbon-based materials such as graphene, carbon nanotube, and their complex 3D composite structures[7-9]. In this study, we utilize the optimized parameters for better agreement with experimental data[10], as these parameters show improved fits to graphene's in-plane phonon-dispersion curves (See Figure S3).

Thermal conductivity

There are two common ways to predict thermal conductivities from MD simulations: equilibrium (Green-Kubo relation) and non-equilibrium MD methods. Both methods have been extensively utilized for determining thermal conductivities of graphene[11, 12] and porous materials[13]. From kinetic theory, thermal conductivity can be expressed as[14]

$$\lambda = \frac{1}{3}\sum_{\omega} c(\omega) v l(\omega) = \frac{1}{3} c(\omega) v^2 \tau(\omega), \qquad \text{(S2)}$$

where $c(\omega)$, v, $l(\omega)$, and $\tau(\omega)$ are the phonon-specific heat, group velocity, MFP, and relaxation time, respectively.

Non-equilibrium molecular dynamics (NEMD)

We relax the systems in the NPT ensemble together with the Langevin thermostat and Berendsen barostat at a low temperature of 10K for the cell parameters. Next, the Nosé-Hoover thermostat is applied to equilibrate the system at 300K for 5ps with a time step of 0.5 fs. Thereafter, the heat flux is imposed in the NVE ensemble for 0.5ns or 1.0ns with 0.25fs (0.5fs for L=15nm and 20nm) time step for the steady state. The short time step is required for conserving the system's total energy while performing ensemble averaging, and the longer relaxation time is required for the longer system to attain a linear temperature gradient. Subsequently, averaged temperature gradients are obtained for 0.5ns. Since a small cross sectional area and heat flux result in large standard deviations of temperature, we set up the system with replicated units for all simulations and scale the heat flux based on the length of the simulation box, which gives a net temperature drop of approximately 10K. Detailed information including lateral dimension, thickness, heat flux and the length is shown in Figure S4. The temperature gradient is obtained by linear regression of the temperature profile of the system at steady state as shown in Figure S5. All temperature gradients of models are shown in Figure S6-10. The thermal conductivity is simply obtained from Fourier's Law:

$$\lambda = -\frac{j}{\partial T / \partial x}, \qquad \text{(S3)}$$

where j and $\partial T / \partial x$ are the heat flux and the temperature gradient respectively.

Equilibrium molecular dynamics (EMD) with Green-Kubo relation

Thermal conductivity in the direction i is given by[15, 16]

$$\lambda_i = \frac{1}{k_B V T^2}\int_0^{\infty} \langle J_i(t) J_i(0)\rangle dt, \qquad \text{(S4)}$$

where k_B, t, V, J_i and $\langle J_i(t) J_i(0)\rangle$ are the Boltzmann constant, time, volume, heat current vector in the i direction and the heat current autocorrelation function (HCACF). The detailed expression of the heat current vector is expressed as[12]

$$J = \sum_i e_i v_i + \frac{1}{2}\sum_{i<j} (f_{ij} \times (v_i + v_j)) x_{ij}, \qquad \text{(S5)}$$

where e_i, v_i, f_{ij} and x_{ij} are the energy, velocity of atom i, forces and distance between atom i and j, respectively. All models are relaxed in the NPT ensemble with the Langevin thermostat and Berendsen

barostat from10K and 300K. Next, sequential NPT, NVT, and NVE ensembles are applied at 300K for 10^6 steps each. Finally, the data of heat flux vectors are accumulated for 10^7 steps with the NVE ensemble. The typical HCACF data and thermal conductivity for graphene as a function of time are shown Figure S11. The HCACF and thermal conductivities of gyroid models are shown in Figure S12.

Acoustic mode relaxtion time

The thermal conductivity of a monatomic crystal can be decomposed into contributions from a fast optical mode and a slow acoustic mode as[17]

$$C_J(t) = \langle J(t) \times J(0) \rangle = A_O \exp(-t/t_O) + A_a \exp(-t/t_a) . \qquad \text{(S6)}$$

Since the contribution of the fast optical modes for the thermal conductivity is usually negligible, it can be simplified as $\kappa = \kappa_0(1 - \exp(-t/t_a))$.

Phonon density of state (PDOS)

The vibrational density of state (vDOS) can be determined from the Fourier transform of the velocity autocorrelation function (VACF) as[18]

$$g(\omega) = \frac{1}{\sqrt{2\pi}} \int e^{i\omega t} \frac{\langle v(t)v(0) \rangle}{\langle v(0)v(0) \rangle} . \qquad \text{(S7)}$$

The phonon density of states (PDOS) is calculated from PDOS $= [g(\omega)]^2$. We note that the noise of PDOS depends on the number of atoms in systems and sampling time. Here, we use more than 20,000 atoms by repeating the unit cell if it is necessary for all samples, and 5ps sampling with 0.25fs time step. From the PDOS ($D(\omega)$), the specific heat can be obtained by,

$$C_V = k_B \int \left(\frac{\hbar\omega}{k_B T} \right)^2 \frac{e^{(\hbar\omega/k_B T)}}{\left[e^{(\hbar\omega/k_B T)} - 1 \right]^2} D(\omega) d\omega . \qquad \text{(S8)}$$

In the integral, the contribution of PDOS is proportional to $(\hbar\omega)^2 e^{\hbar\omega/k_B T} \left[e^{(\hbar\omega/k_B T)} - 1 \right]^{-2}$. In the current study at 300K, the contribution of 50THz is only 2.5% of that of 10THz.

Normalization and dissipation factor of atomic heat flux

We average 400 points during 500ps of steady states of NEMD. From the summation of the vector in the heat flux direction and the system length, the net flux per unit length is obtained as

$$J_{uy} = \sum_i J_{iy} / l_y , \quad (12)$$

where J_{iy} and l_y are the component of the heat flux vector and the system length in the heat flux direction (the y direction), respectively. The normalized spatial distribution of the atomic heat flux can be obtained by

$$J_{nor} = \frac{\sqrt{J_{ix}^2 + J_{iy}^2 + J_{iz}^2}}{J_{uy}} . \qquad \text{(S9)}$$

This normalization allows all different systems to have the same net heat flux per unit system length in the direction of heat flux. Next, we define the dissipation factor (D) by

$$D = \frac{1}{J_{net}} \sqrt{\frac{\sum_i J_{nor}^2}{N}} \quad . \qquad \text{(S10)}$$

Respectively, N and J_{net} are the number of atoms and the norm of the net flux of the system from J_{nor}. This dissipation factor represents the localized heat flux that does not contribute to the net flux in NEMD. For visualization of atomic heat flux vectors, we utilize the normalized components as

$$J = \left(J_{i\bar{x}}, J_{i\bar{y}}, J_{i\bar{z}} \right) = \left(\frac{J_{ix}}{J_{uy}}, \frac{J_{iy}}{J_{uy}}, \frac{J_{iz}}{J_{uy}} \right). \qquad \text{(S11)}$$

We utilize AtomEye[19] and VMD[20] for visualization.

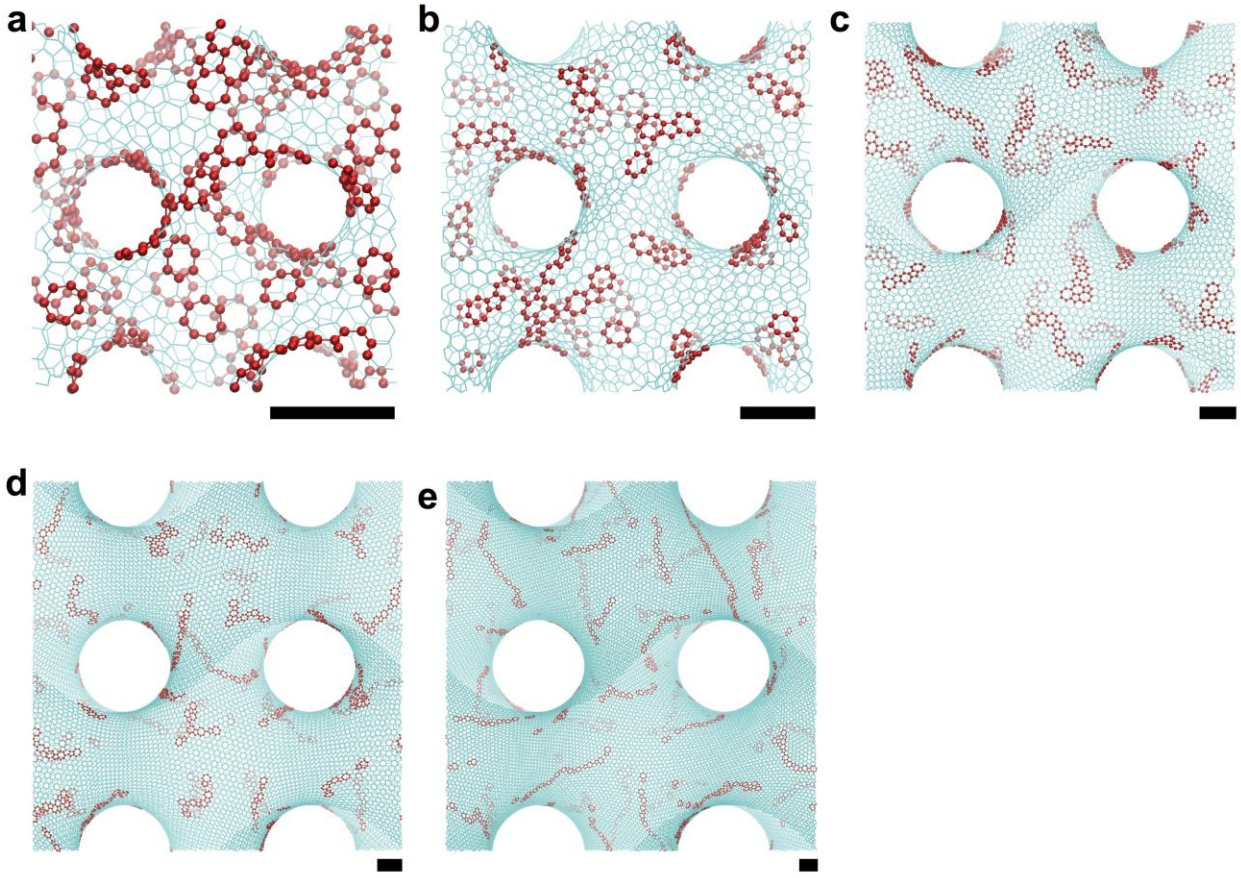

Figure S1. **a-f**. The spatial distribution of defects in the gyroid models: L= 3, 5, 10, 15 and 20nm. Red atoms indicate the atoms belong to non-hexagonal ring defects. The scale bar represents 1nm for each model.

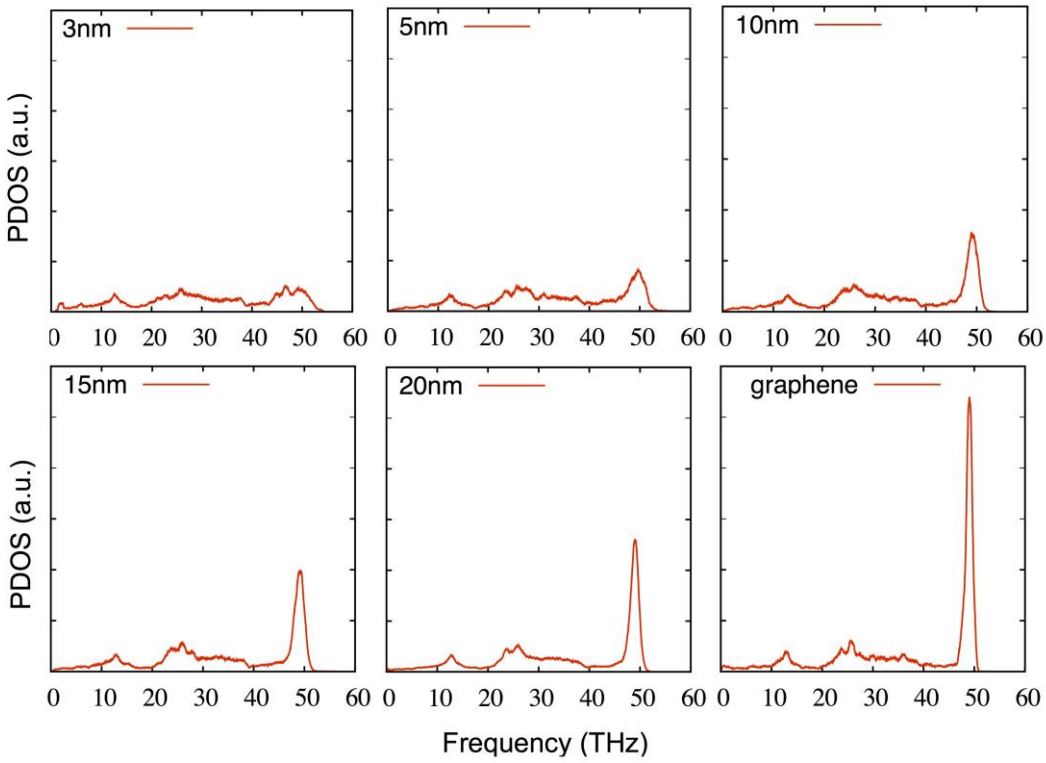

Figure S2. Phonon density of states of gyroid graphene and graphene (Separated images)

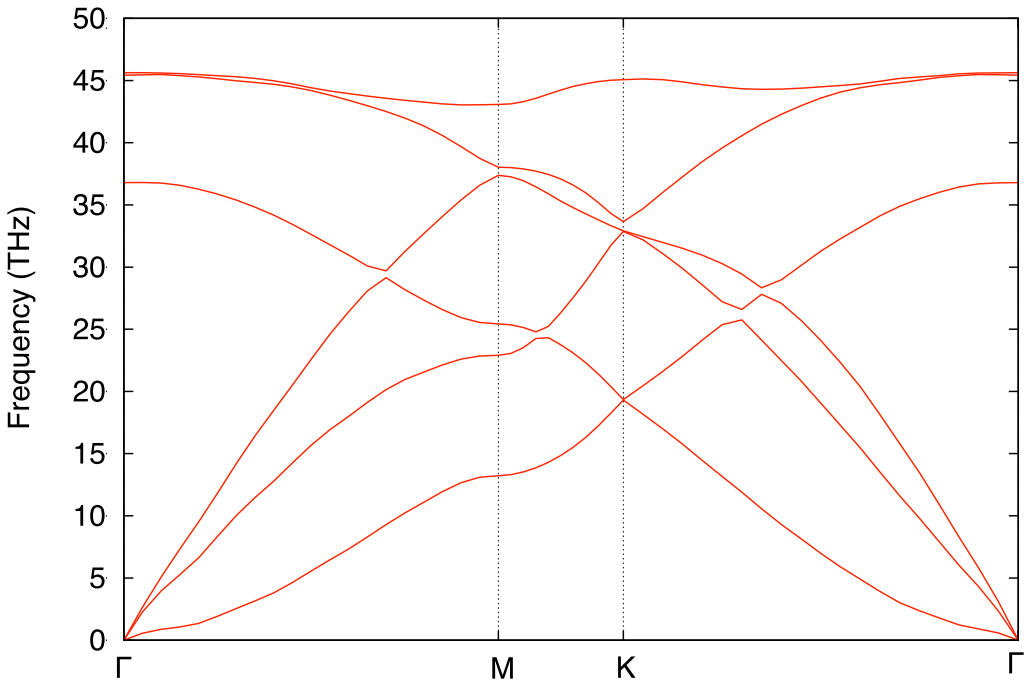

Figure S3. Phonon dispersion curves of graphene (10nm x 10nm) obtained from lattice dynamics with the optimized Tersoff potential[21].

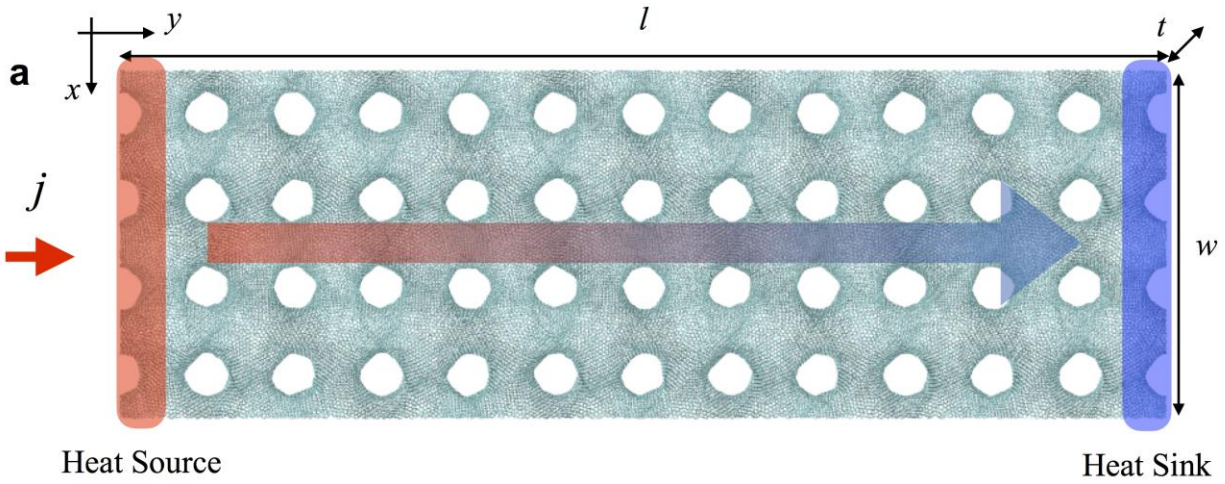

b

L (nm)	3	5	10	15	20
l (nm)	3,6,15,30,60	5,10,20,30,40,60	10,20,30,40,60	15,30,45,60,75,90	20,40,60,80,100
w (nm)	9	10	20	15	20
t (nm)	9	10	10	15	20
j (eV/ps)	0.4 ~ 8.0	0.5 ~ 4.0	1.0 ~ 4.0	0.6 ~ 2.8	1.0 ~ 5.0

Figure S4. **(a)** An example of the NEMD setup with a gyroid model (L=10nm) for l = 60nm, w=20nm, and t=10nm. **(b)** The table of the detailed NEMD configurations for all models. The heat flux energy, j, is selected based on the temperature gradient. Also, the cross-sectional areas (wt) are selected based on the standard deviation of temperatures of the temperature gradient.

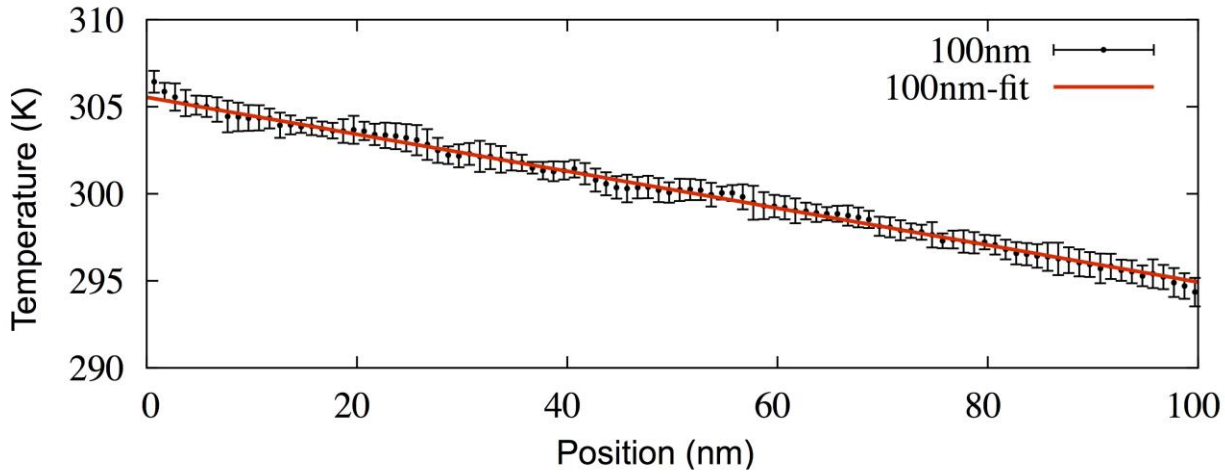

Figure S5. Typical temperature distribution of gyroid graphene with *L*=20nm and *l*=100nm)

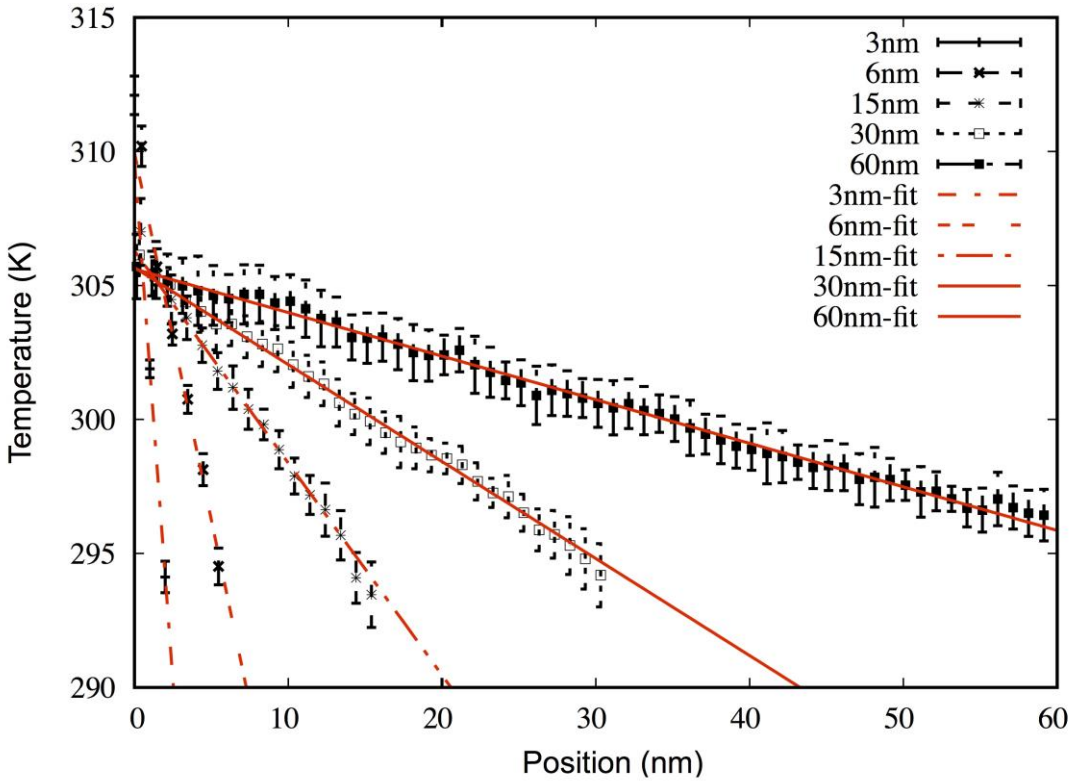

Figure S6. Temperature distribution of gyroid graphene with *L*=3nm with various lengths.

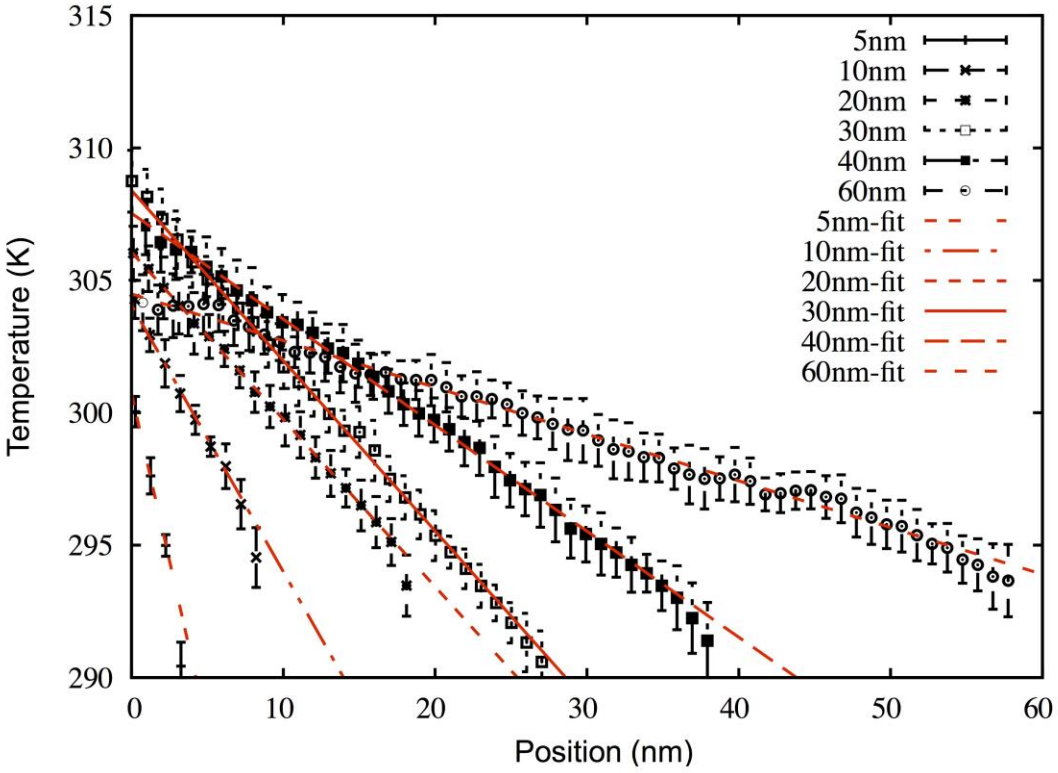

Figure S7. Temperature distribution of gyroid graphene with *L*=5nm with various lengths.

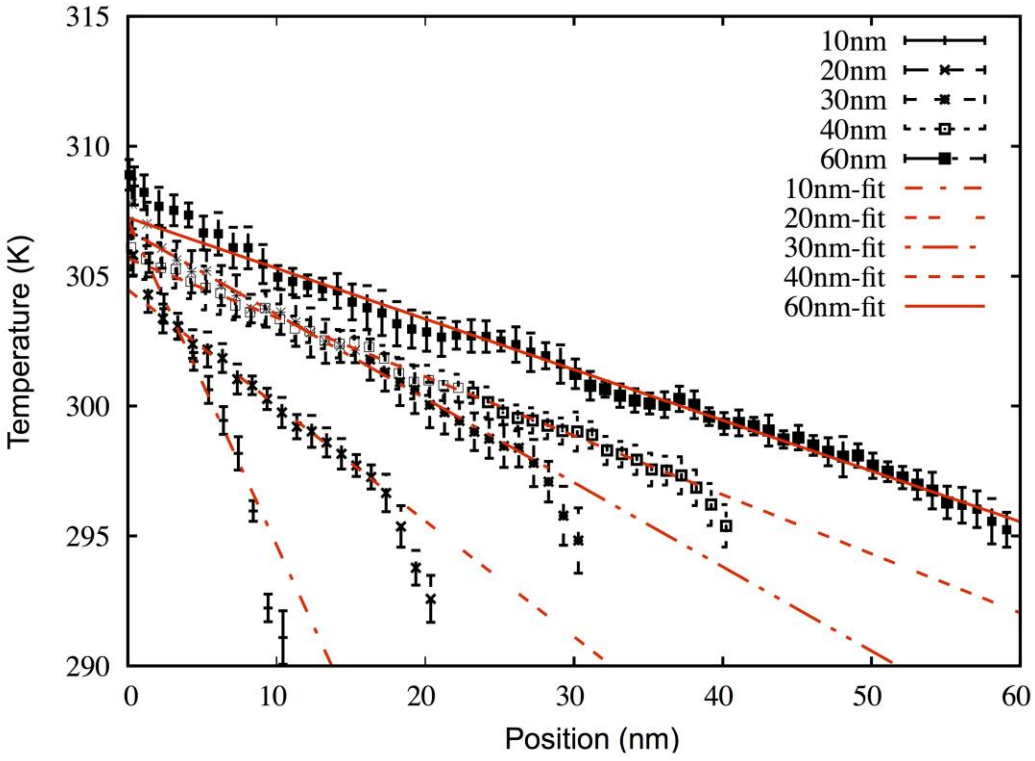

Figure S8. Temperature distribution of gyroid graphene with *L*=10nm with various lengths.

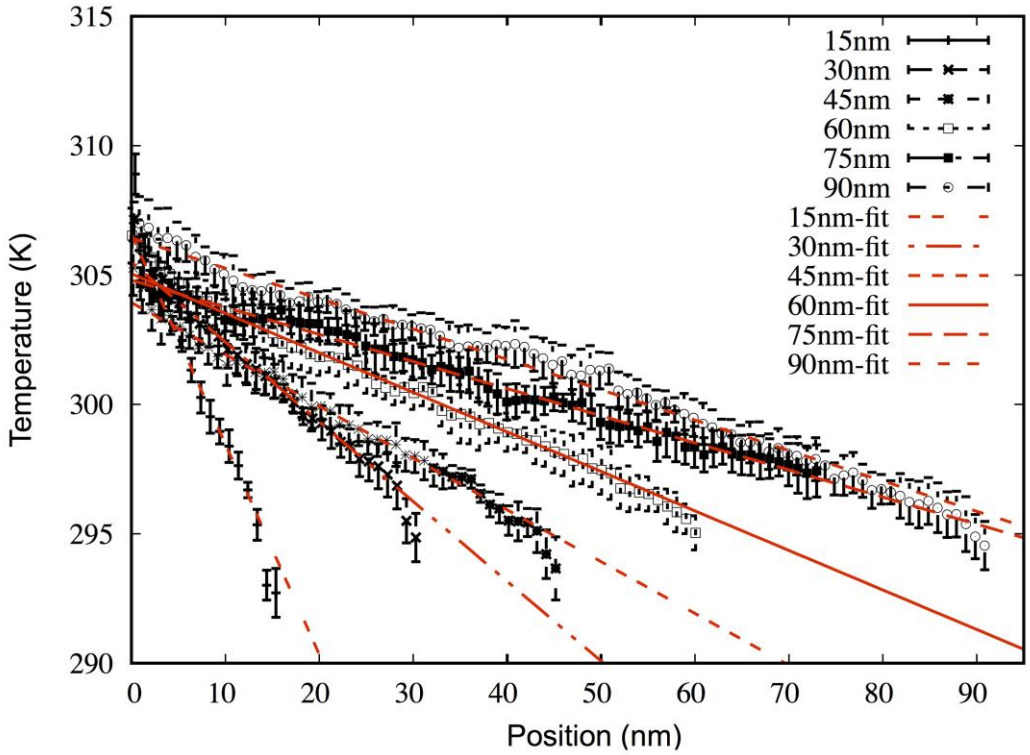

Figure S9. Temperature distribution of gyroid graphene with *L*=15nm with various lengths.

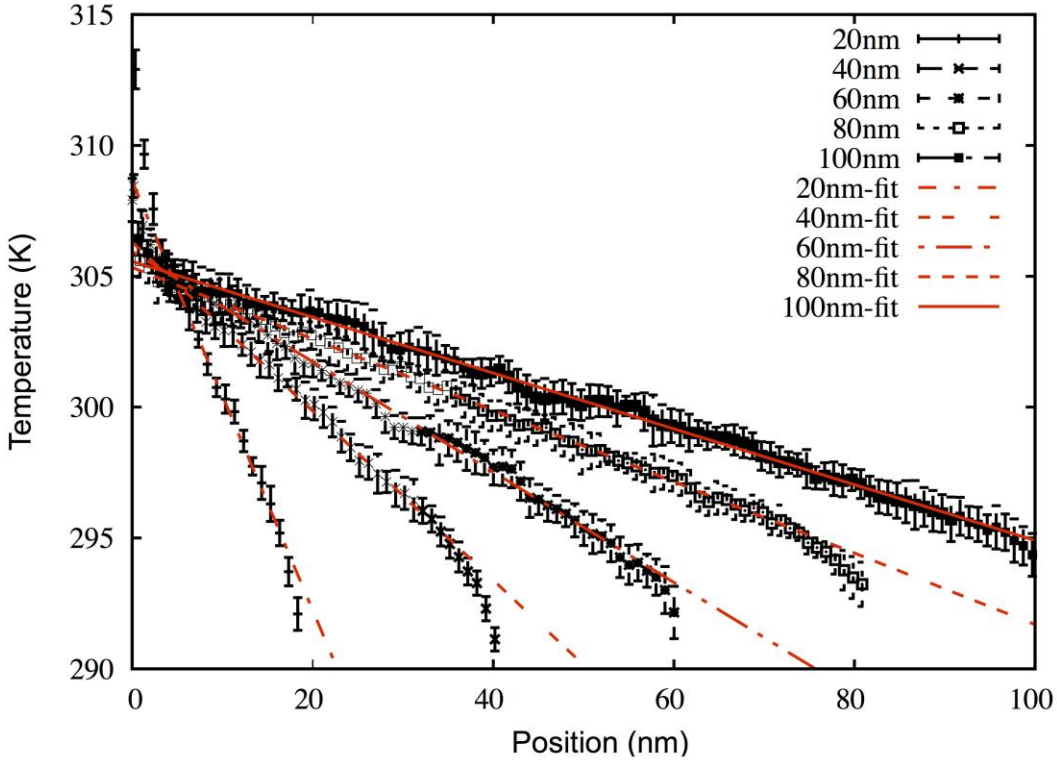

Figure S10. Temperature distribution of gyroid graphene with *L*=20nm with various lengths.

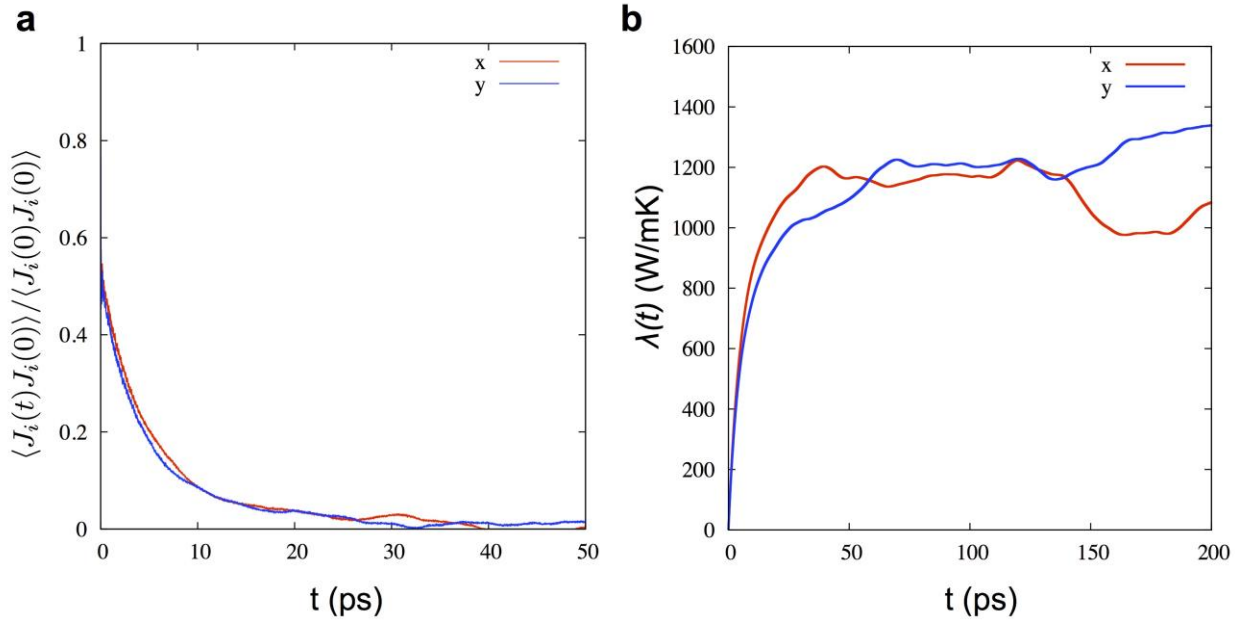

Figure S11. The HCACF (**a**) and thermal conductivity (**b**) and from EMD (Green-Kubo) of graphene (10nm x 10nm).

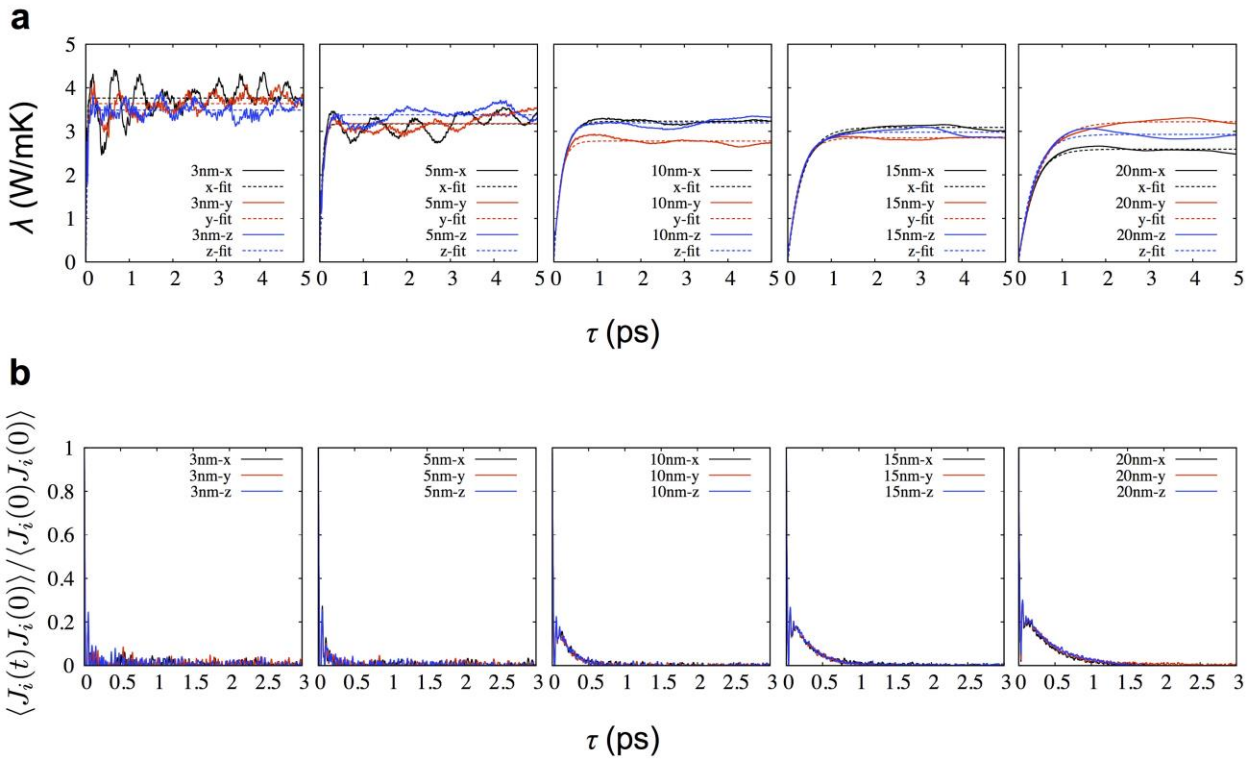

Figure S12. The thermal conductivity (**a**) and HCACF (**b**) from EMD (Green-Kubo) of gyroid graphene.

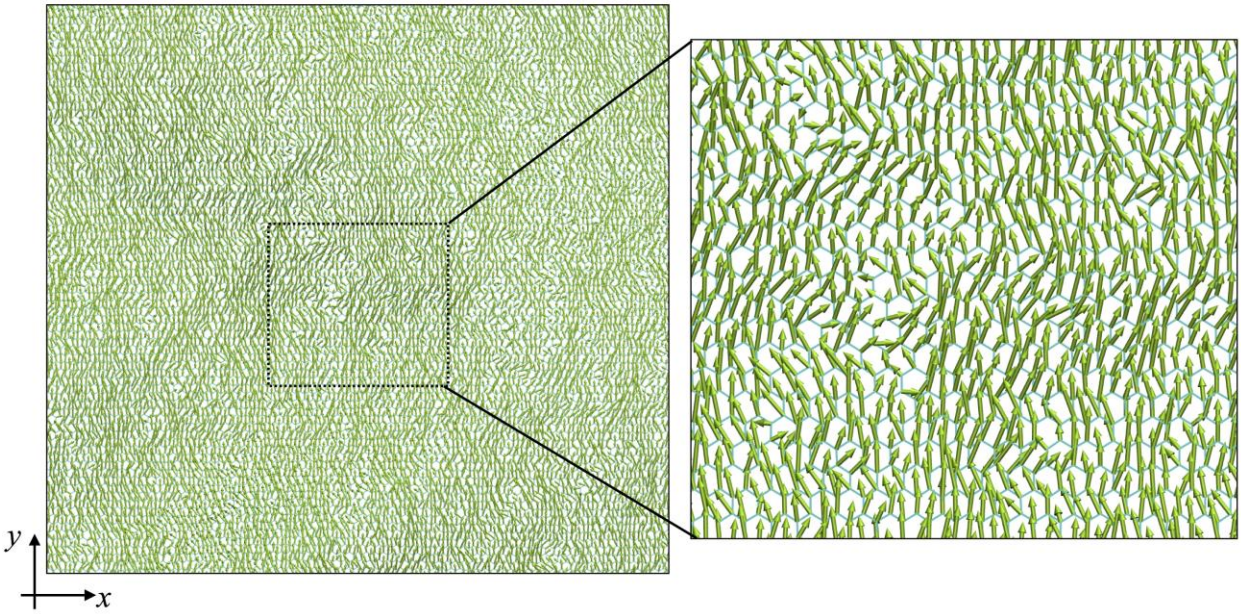

Figure S13. Atomic heat flux vectors of graphene: homogeneous distribution and clear directionality in the heat flux direction (in the *y* direction)

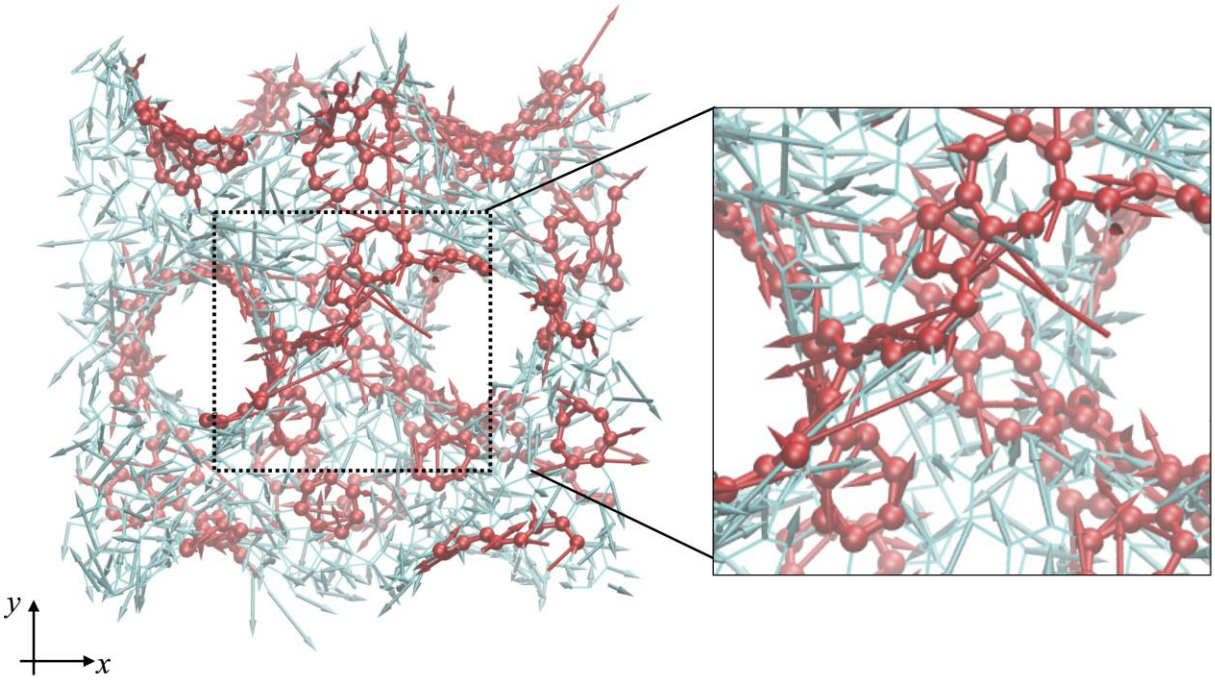

Figure S14. Atomic heat flux vectors of gyroid model (L=3nm), NEMD applied in the y direction: non-homogeneous and complicated directionality. The red atoms indicate defects. The vectors of hexagonal atoms show large variation as those of detect atoms.

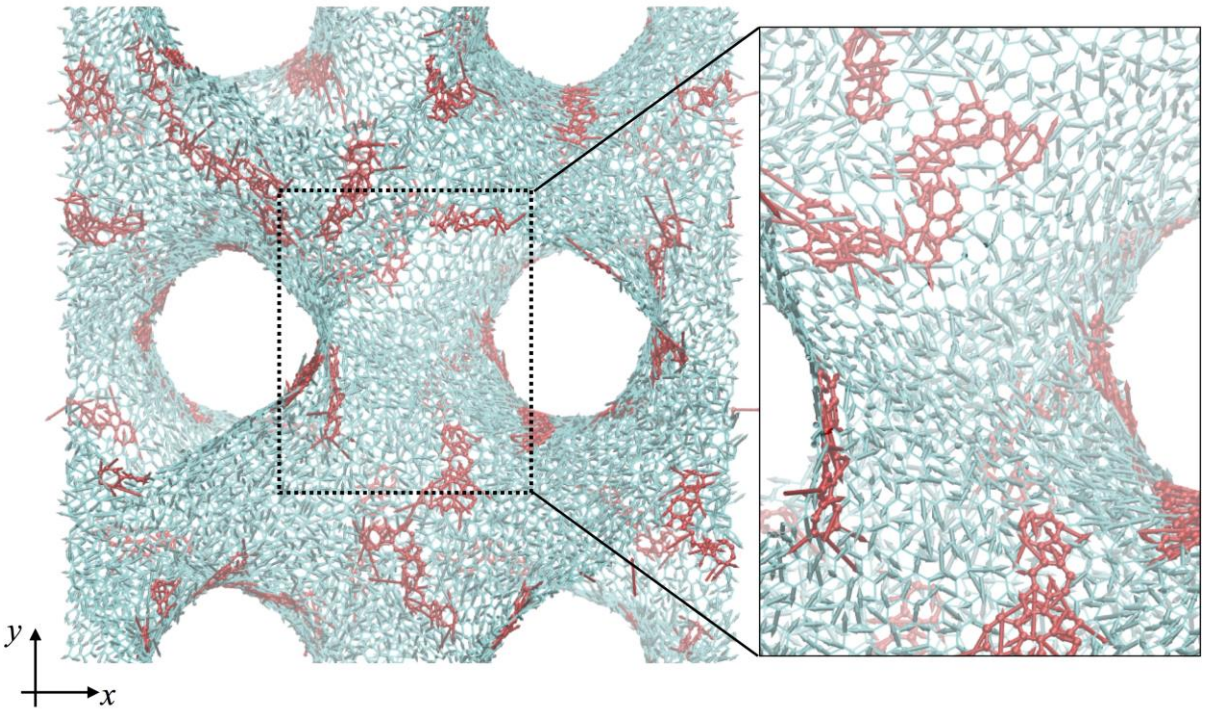

Figure S15. Atomic heat flux vectors of gyroid model (L=10nm), NEMD applied in the y direction: The red atoms indicate defects. The vectors of hexagonal atoms show slightly less deviation than those of 3nm model. The directionality is still unclear.

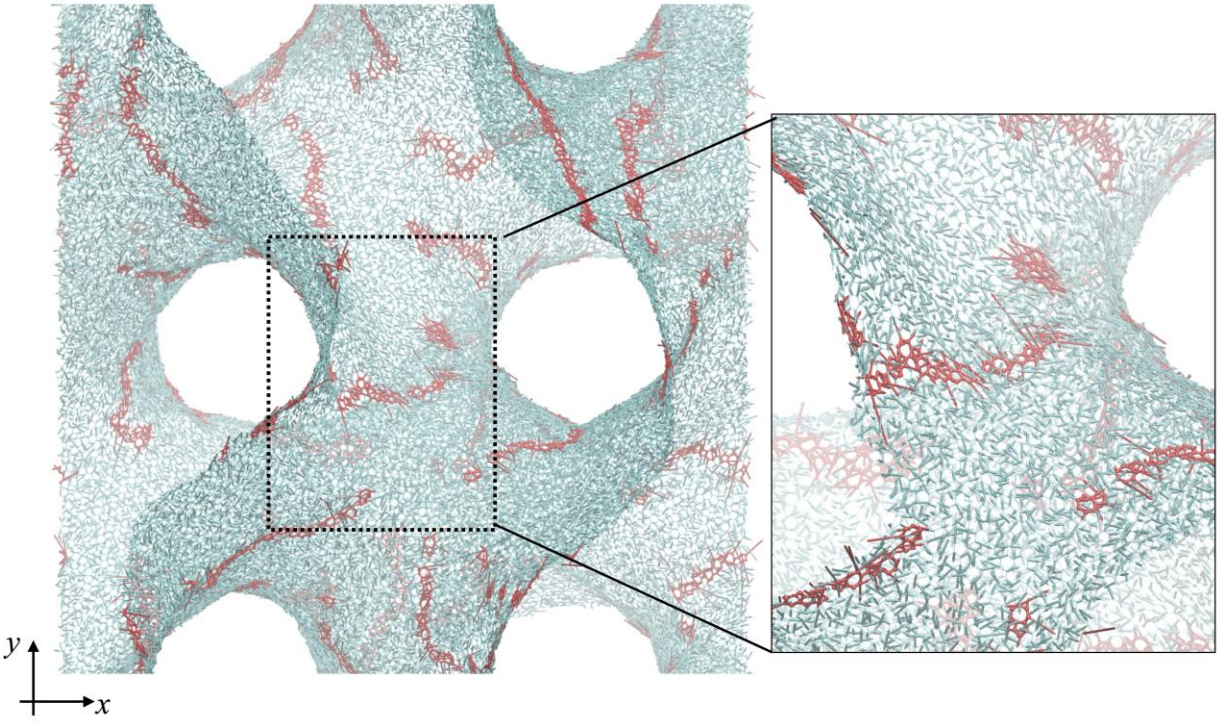

Figure S16. Atomic heat flux vectors of gyroid model (L=20nm), NEMD applied in the y direction: The red atoms indicate defects. The vectors of hexagonal atoms show much less deviation than those of

hexagonal atoms, clearly showing the difference between defects and hexagonal atoms. The directionality is still unclear because the vector basically follows the lattice directions.

Table S1. Defect types and disorder ratios of three-dimensional gyroid graphene models.

***L* (nm)**	**5 rings**	**6 rings**	**7 rings**	**8 rings**	**Disorder ratio by #type (%)**	**Disorder ratio (*β*) by #atom (%)**
3	17	439	64	0	15.58	41.0
5	30	1002	70	0	9.07	18.8
10	147	5635	192	1	5.69	13.0
15	279	12896	321	3	4.47	10.0
20	473	23086	413	4	3.71	9.0

Table S2. Fitted parameter data for thermal conductivity (exponential fit), $\kappa(x) = \kappa_0(1 - \exp(-x/l_0))$, and inversed thermal conductivities (inverse linear fit), $\frac{1}{\kappa}\left(\frac{1}{x}\right) = A\left(\frac{1}{x}\right) + \frac{1}{\kappa_0}$, as a function of the length and inversed length from NEMD.

***L* (nm)**	**λ_0 (W/mK)**	**l_0 (nm)**	***A***	**Λ_0 (W/mk)**
3	4.45	58.9	9.66	4.94
5	4.15	84.0	8.46	4.50
10	3.74	88.15	15.82	4.19
15	3.75	157.7	26.66	4.14
20	3.57	200.5	36.52	4.1

Table S3. Fitted parameter data for thermal conductivity (exponential fit), $\kappa(x) = \kappa_0(1 - \exp(-x/t_0))$ as a function of correlation time (ps) from EMD (zz: zigzag direction, ac: armchair direction). The parameter, τ_0, is a relaxation time of the fast acoustic modes. The size effects are tested with doubled size

***L* (nm)**	**λ_0 (W/mK)**	**τ_0 (ps)**	***Doubled size* λ_0 (W/mK)**
3	3.62 ± 0.14	0.02	3.52 ± 0.03
5	3.25 ± 0.12	0.07	3.07 ± 0.15

10	3.07 ± 0.25	0.17	3.00 ± 0.07
15	2.97 ± 0.11	0.29	2.91 ± 0.09
20	2.91 ± 0.32	0.37	2.69 ± 0.15
Reference (graphene)	1218 (zz), 1121(ac)	8.78	-

Table S4. The effects of width and thickness. We have tested doubled width or thickness with the longest sample in the *y* direction (*l*). The results show the thermal conductivities from the Fourier law. Increasing the width or thickness from the current setting does not affect thermal conductivities.

***L* (nm)**	***λ (t, w, l)***	***λ_{tested} (t, w, l)***
3	4.71 ± 0.47 (9,9,60)	5.08 ± 0.39 (18,9,60)
5	4.64 ± 0.44 (10,10,60)	4.32 ± 0.31 (20,10,60)
10	4.03 ± 0.38 (20,10,60)	3.73 ± 0.17 (20,20,60)
15	3.99 ± 0.4 (15,15,90)	4.07 ± 0.48 (30,15,90)
20	3.7 ± 0.46 (20,20,100)	3.2 ± 0.2 (40,20,100)

Table S5. Temperature dependency obtained from EMD with doubled sizes due to their small standard deviations. Fitted data for thermal conductivity (exponential fit), $/(x) = /_0(1 - \exp(-x/t_0))$ as a function of correlation time (ps) from EMD. The dependency parameter, α, is fitted to $\lambda \sim T^{\alpha}$ in the range between 200K to 400K.

***L* (nm)**	**λ_0 (W/mK) @200K**	**λ_0 (W/mK) @300K**	**λ_0 (W/mK) @400K**	**α**
3	3.65 ± 0.14	3.52 ± 0.03	3.49 ± 0.07	0.005
10	3.19 ± 0.04	3.00 ± 0.07	2.98 ± 0.04	0.008
20	2.77+0.1	2.69 ± 0.15	2.64 ± 0.02	0.06

Reference

1. S. Plimpton, *J Comput Phys*, 1995, **117**, 1-19.
2. Z. Qin, G. S. Jung, M. J. Kang and M. J. Buehler, *Sci. Adv.*, 2017, **3**, e1601536.
3. D. W. Brenner, O. A. Shenderova, J. A. Harrison, S. J. Stuart, B. Ni and S. B. Sinnott, *J Phys-Condens Mat*, 2002, **14**, 783-802.
4. S. J. Stuart, A. B. Tutein and J. A. Harrison, *J Chem Phys*, 2000, **112**, 6472-6486.
5. S. Wang, Z. Qin, G. S. Jung, F. J. Martin-Martinez, K. Zhang, M. J. Buehler and J. H. Warner, *ACS Nano*, 2016, **10**, 9831-9839.
6. G. S. Jung, Z. Qin and M. J. Buehler, *Extreme Mechanics Letters*, 2015, **2**, 52-59.
7. J. J. Yeo and Z. Liu, *Journal of Computational and Theoretical Nanoscience*, 2014, **11**, 1790-1796.
8. J. Tersoff, *Phys. Rev. B*, 1989, **39**, 5566-5568.

9. J. Tersoff, *Phys. Rev. B*, 1988, **37**, 6991-7000.
10. L. Lindsay and D. A. Broido, *Phys. Rev. B*, 2010, **81**, 205441.
11. D. L. Nika and A. A. Balandin, in *Thermal Transport in Low Dimensions: From Statistical Physics to Nanoscale Heat Transfer*, ed. S. Lepri, Springer International Publishing, Cham, 2016, DOI: 10.1007/978-3-319-29261-8_9, pp. 339-363.
12. M. H. Khadem and A. P. Wemhoff, *Comput. Mater. Sci.*, 2013, **69**, 428-434.
13. J. Yeo, Z. Liu and T. Ng, *Modelling and Simulation in Materials Science and Engineering*, 2013, **21**, 075004.
14. Y. Wang, Z. Song and Z. Xu, *J. Mater. Res.*, 2014, **29**, 362-372.
15. R. Kubo, *Rep. Prog. Phys.*, 1966, **29**, 255-284.
16. R. Kubo, M. Yokota and S. Nakajima, *J. Phys. Soc. Jpn.*, 1957, **12**, 1203-1211.
17. J. Che, T. Çağın, W. Deng and W. A. Goddard Iii, *J. Chem. Phys.*, 2000, **113**, 6888-6900.
18. P. H. Wu, S. S. Quek, Z. D. Sha, Z. L. Dong, X. J. Liu, G. Zhang, Q. X. Pei and Y. W. Zhang, *J. Appl. Phys.*, 2014, **116**, 204303-204307.
19. J. Li, *Journal*, 2003, **11**, 173.
20. W. Humphrey, A. Dalke and K. Schulten, *J. Mol. Graphics*, 1996, **14**, 33-38.
21. L. T. Kong, *Comput. Phys. Commun.*, 2011, **182**, 2201-2207.